PERGAMON

International Journal of Multiphase Flow 27 (2001) 1803–1827

International Journal of Multiphase Flow

www.elsevier.com/locate/ijmulflow

Constitutive parameters for liquid-fluidized beds

James C. Jin, Charles S. Campbell *

Department of Mechanical Engineering, University of Southern California, Los Angeles, CA 90089-1453, USA

Received 29 June 2000; received in revised form 23 March 2001

Abstract

The constitutive parameters (particulate phase effective elasticity, particulate effective viscosity, added mass coefficient and drag gradient) in an unstable liquid-fluidized bed are determined as functions of voidage and slip velocity. To identify these system parameters, first, forced instability wave properties are measured in water-fluidized beds, then an optimum parameter identification method is developed to reliably determine these system parameters based on a generic instability model. The results give some insight into the internal mechanics of liquid-fluidized beds and are compared with other models when they are available.

Keywords: Fluidized beds; Instability; Constitutive parameters

1. Introduction

In fluidized bed stability analyses, the fundamental governing equations usually involve many undetermined constitutive parameters representing the particle–particle and fluid–particle interaction forces (Homsy et al., 1980; Jackson, 1985; Anderson and Jackson, 1968b; El-Kaissy and Homsy, 1976; Ham et al., 1990; Foscolo and Gibilaro, 1987, among others). There have been attempts to determine these properties from first principles (e.g. Koch and Sangani, 1999) but little data are available on which to evaluate their success. The particle–particle interaction forces which are generally represented by, or at least can be put in the form of, a particle effective elasticity and a particle effective viscosity and the fluid–particle interaction forces which are generally represented as drag and added mass forces. Because of the difficulties of experimentally measuring these quantities, only a few pioneering studies have been performed.

* Corresponding author. Tel.: +213-740-0498; fax: +213-740-8071.
E-mail address: campbell@usc.edu (C.S. Campbell).

0301-9322/01/$ - see front matter
PII: S0301-9322(01)00024-6

Schügerl et al. (1961) carried out experimental measurements of the effective viscosity in a gas-fluidized bed particle phase using a cylindrical Couette rheometer. The measured values (see the summary by Clift and Grace, 1985) are in the range of several to ten's poise which are much higher than those typically found in particle suspensions (eg. Thomas, 1965). Similar values were determined by Grace (1970) from the rise velocity of bubbles in gas-fluidized beds. Anderson and Jackson (1968a) also predicted that the corresponding particle phase viscosity for a liquid-fluidized bed would be the same order as a gas-fluidized bed.

Direct particle pressure measurements were performed by Campbell and Wang (1991) in a gas-fluidized bed. They measured the particle pressure exerted on the sidewall over the entire range between a packed bed and a fully fluidized slugging bed. This measurement showed that the particle pressure initially decreases with increasing fluid velocity due to the increasing support of the bed by fluid forces, but after minimum fluidization it will increase, reflecting the effect of bubbles. It was found that the particle pressure is proportional to particle density and bubble size for a fully fluidized bed. In liquid-fluidized beds, Kumar et al. (1990) used a hydrophone mounted in the wall to "listen" for the individual particle impacts, and to infer the pressure from the frequency and strength of the impacts. More sophisticated measurements along the same lines were performed by Zenit et al. (1997). The resultant particle pressure in liquid-fluidized beds is much smaller than those found in gas-fluidized beds.

Ham et al. (1990) reports the only elasticity measurements in liquid-fluidized beds that have been reported so far. The elasticity measurement was based on determining the onset of instability and filtering the results through Batchelor's (Batchelor, 1988) stability model. To use this stability criterion to measure the elasticity, appropriate drag models, a virtual mass model and a mobility model had to be chosen, so that the determined elasticities are dependent on the accuracy of these models. The results of these measurements showed that particle elasticity is a function of particle Reynolds number and fluid/solid density ratio.

Rietema (1991) uses a similar scheme to determine the elasticity of gas-fluidized fluid cracking catalyst (FCC) powders. The physics here are vastly different than in liquid-fluidized beds as for FCC the elasticity arises largely from interparticle forces. In gas-fluidized beds disturbances grow so rapidly that regions of linear instability are not observed and instead bubbles form almost immediately. This makes the determination of the elasticity somewhat more direct as bubbles are only stabilized by the elasticity and it is not necessary to assume models for the other parameters. Conversely, the experiments also yield no knowledge about the other parameters.

There are several popular drag models, such as Ergun (1952), Richardson and Zaki (1954) and Foscolo and Gibilaro (1987), but their accuracy for use in stability analyses has not yet been determined. For the added mass effect, there are some theoretical studies to establish the relationship between added mass coefficient and other parameters such as void fraction (Drew et al., 1979; Atkinson and Kytomaa, 1992; Guo and Chwang, 1992; Lamb, 1945), but the predicted values still vary significantly among the models, and there are no measurements to support any one model over any other.

To further understand the constitutive behavior of fluidized systems, it will be necessary and important to determine particle–particle interaction forces and fluid–particle interaction forces from an experimental point of view.

There have been attempts to do this in the past. Anderson and Jackson 1969, assumed the form of the drag law and the value of the added mass coefficient, and assessed the other constitutive

parameter. Homsy et al. (1980) did much the same assuming only the form of the drag law. The work presented here is somewhat more extensive and makes no assumptions about any constitutive parameters. To achieve this goal, we experimentally measured forced instability waves, and we then separately derive general governing equations without making assumptions about any of the terms (drag forces, added mass effect, particulate effective elasticity and particulate effective viscosity) which normally must be modeled, yielding a "generic stability analysis". Finally, an Optimum Parameter Identification Method is developed to yield values for the constitutive terms by combining the forced wave instabilities with the generic model. The comparison of the results with the predictions from available models will give a judgment on their appropriateness, at least for use in stability analyses.

2. Methodology

2.1. Forced waves in fluidized bed

Instability measurements are made in the 190 mm long by 25 mm diameter cylindrical fluidized bed shown in Fig. 1. The distributor is a porous plate composed of 20 μm particles. This ensures a

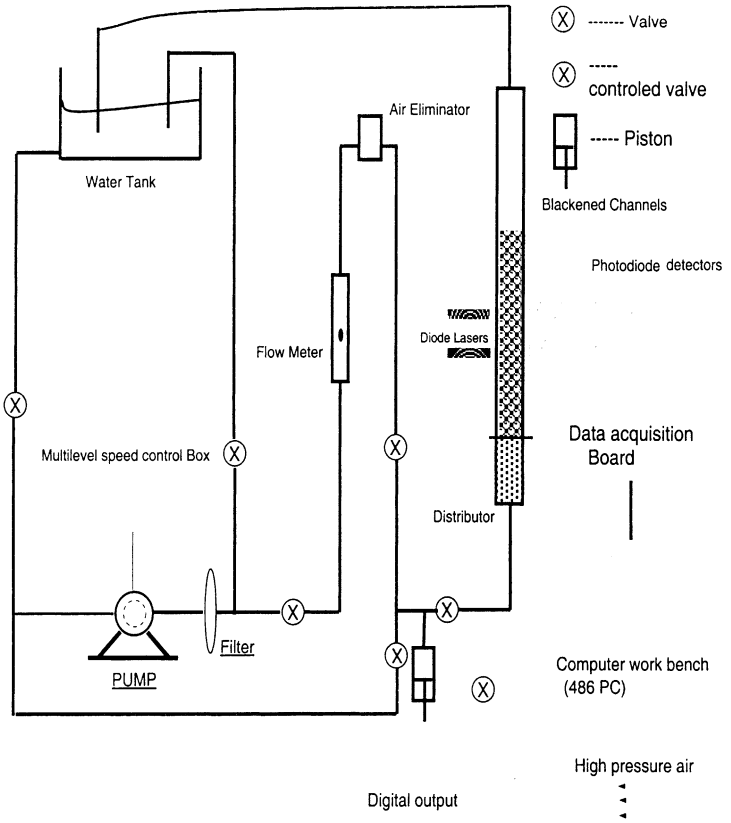

Fig. 1. A schematic of experimental apparatus.

large pressure drop across the plate and thus, a nearly uniform fluidization velocity. The instantaneous concentration is determined using a light attenuation technique similar to ones used by Anderson and Jackson (1968a,b) and El-Kaissy and Homsy (1976). A constant intensity light is provided by two small ALS 4 mW diode lasers. Each signal is sensed by a Melles–Griot silicon photodiode that is placed at the end of a 6 mm diameter and 20 mm long cylindrical channel that has been painted black to minimize noise from scattered light. The 35.56 mm spacing between the two measurement points was chosen by trial and error to eliminate cross talk between the channels. The attenuation of each beam provides an instantaneous measurement of the particle concentration and cross-correlating the signals provides the time delay used to determine the wavespeed. To compensate for the greater attenuation for the smaller beads, and allow the use of the same light source and photodiode detectors, a smaller 1.27 cm diameter bed was used for 0.5 mm glass beads.

One difficulty with all light attenuation systems is making an accurate calibration against concentration. In particular, the problem is to create a system with a known particle concentration upon which such a calibration might be based. We have developed a technique that nearly eliminates this uncertainty by basing the calibration, not on the local concentration which is somewhat uncertain, but on the total volume of particles in the bed, (which is easily determined from the weight of particles divided by their density), compared against the concentration signal integrated along the axial length of the bed. See the description in Jin (1996) for more details.

The goal of this project was to determine appropriate constitutive parameters for inclusion in fluidized bed stability theories. This is done by solving the inverse instability problem based on measured values of the linear growth rates, frequencies and wavespeeds in the apparatus shown in Fig. 1. To obtain strong waves at a given frequency, the waves are forced by fluctuating the superficial velocity either by varying the pump speed or by a piston located near the inlet of the fluidized beds. The initial measurements were made with instabilities generated by varying the pump speed. However, it was found that we could not observe instabilities at high (i.e. a few Hz) frequencies and it was not clear whether this was natural feature of the fluidized beds or was a byproduct of the pump's inertia slowing the response to the applied frequency. Consequently, we tried an alternate forcing technique that utilized a pneumatically driven piston which had a better frequency response. But, it turned out that there were no apparent differences between the two forcing schemes which indicated that the limited frequency response was a natural feature of the beds that were studied.

For this type of inverse problem, the more information that is available, the more accurate the results. Thus, in addition to the forced wave measurements, we also obtained some supplemental growthrate information by probing the generated instabilities for other frequencies (other than the forced frequency) that are generated spontaneously within the fluidized bed but still demonstrated linear growth. Such signals are identified by passing the signal through a digital notch filter with a 1% width. When the amplitude of such a signal shows linear growth in the region near the distributor, then that extra growthrate is used in determining system parameters. During the process, it is found that arbitrarily chosen frequencies do not always exhibit a region of clear linear growth, even near the distributor, so many possible frequencies must be considered to obtain these supplemental growthrates.

Tables 1 and 2 show the properties of the beds and the glass beads used in the experiments.

Table 1
Glass properties used in the experiments

Set no.	Glass beads	ρ_p (Kg/m^3)	d_p (mm)	Dominant, d_p (mm)
A	Potters B	2500	0.5–0.6	0.5
B	Potters A100	2523	1.0–1.18	1
C	Potters A200	2485.7	1.4–2	2

Table 2
Fluidized bed configuration used in the experiments

Set. no.	Dominant, d_p (mm)	Bed diameter, D (mm)	Ratio, D/d_p	$u_{m,f}$ (cm/s)	ε_{mf}
A	0.5	12.7	25.4	0.52	0.389
B	1	25.4	25.4	1.07	0.402
C	2	25.4	12.7	2.65	0.402

Table 3
Wave properties and flowing conditions for set A

f (Hz)	σ (1/cm)	U (cm/s)	ε_0	u_0 (cm/s)
1.0	0.049359	2.57		
1.434	0.067874	–	0.530	1.08
1.988	0.040178	–		
1.0	0.043851	2.62		
1.522	0.069034	–	0.536	1.12
2.287	0.029238	–		
1.0	0.039104	2.66		
1.777	0.074220	–	0.541	1.15
2.393	0.039870	–		
1.0	0.038406	2.69		
1.496	0.070388	–	0.546	1.17
2.530	0.055700	–		
1.0	0.037000	2.72		
1.706	0.068454	–	0.551	1.20
2.701	0.025500	–		

The wave properties are obtained in regions that demonstrated linear growth and for which the wavespeeds and frequencies are also stable. The wave properties for set A are summarized in Table 3. One wavespeed is measured, but three growthrates corresponding to three forcing frequencies were obtained for every voidage in this set. (The wavespeed does not change greatly which, as will be explained in the following section, leads to an ill-conditioned problem. Thus, few wavespeeds are used, or needed, for the inverse problem.) Table 4 shows the wave properties of five runs for set B; here two wavespeeds and three growthrates are measured for every voidage.

Table 4
Wave properties and flowing conditions for set B

f (Hz)	σ (1/cm)	U (cm/s)	ε_0	u_0 (cm/s)
0.740	0.052364	4.11		
1.0	0.065300	3.96	0.485	1.71
1.314	0.033997	–		
0.800	0.049600	4.28		
1.434	0.119980	3.99	0.495	1.76
2.002	0.037518	–		
1.205	0.093600	4.70		
1.795	0.160700	4.34	0.508	1.93
2.361	0.080050	–		
0.801	0.037000	5.01		
2.00	0.157620	4.41	0.516	2.05
2.525	0.050895	–		
1.434	0.086380	5.01		
2.00	0.149400	4.64	0.526	2.15
3.10	0.055729	–		

Table 5
Wave properties and flowing conditions for set C

f (Hz)	σ (1/cm)	U (cm/s)	ε_0	u_0 (cm/s)
0.756	0.06000	4.91		
1.240	0.01102	4.56	0.471	3.46
1.070	0.04330	–		
0.800	0.06508	5.22		
1.522	0.03265	4.80	0.481	3.61
1.170	0.07780	–		
0.792	0.07842	5.59		
1.794	0.15245	5.03	0.496	3.87
2.420	0.08894	–		
0.765	0.05606	5.88		
2.00	0.17918	5.31	0.507	4.06
3.421	0.08876	–		

Table 5 shows the wave properties for set C; here two wavespeeds and three growthrates are measured for every voidage in set C.

2.2. Optimum parameter identification method (OPIM)

2.2.1. Governing equations for the fluidized beds

The continuum approach has been the backbone of fluidization theory. The standard type of model utilizes separate continuity equations and two momentum equations for the solid and fluid

phases. Without any modeling of force terms, they can be written in a manner similar to that of Jackson (1985) for one-dimensional flow.

2.2.2. Conservation of mass

Fluid phase:

$$\frac{\partial \varepsilon}{\partial t} + u_{\mathrm{f}} \frac{\partial \varepsilon}{\partial z} + \varepsilon \frac{\partial u_{\mathrm{f}}}{\partial z} = 0. \tag{1}$$

Particle phase:

$$-\frac{\partial \varepsilon}{\partial t} - u_{\mathrm{p}} \frac{\partial \varepsilon}{\partial z} + (1-\varepsilon) \frac{\partial u_{\mathrm{p}}}{\partial z} = 0. \tag{2}$$

2.2.3. Conservation of momentum

Fluid phase:

$$\rho_{\mathrm{f}} \varepsilon \left(\frac{\partial u_{\mathrm{f}}}{\partial t} + u_{\mathrm{f}} \frac{\partial u_{\mathrm{f}}}{\partial z} \right) = \varepsilon \frac{\partial (T_{\mathrm{f}} - F_{\mathrm{I}} + F_{\mathrm{bf}})}{\partial z}. \tag{3}$$

Particle phase:

$$\rho_{\mathrm{p}} (1-\varepsilon) \left(\frac{\partial u_{\mathrm{p}}}{\partial t} + u_{\mathrm{p}} \frac{\partial u_{\mathrm{p}}}{\partial z} \right) = (1-\varepsilon) \frac{\partial (T_{\mathrm{f}} + F_{\mathrm{I}} + F_{\mathrm{bp}})}{\partial z} + E_{\mathrm{p}} \frac{\partial \varepsilon}{\partial z} + \varepsilon \eta_{\mathrm{p}} \frac{\partial^2 u_{\mathrm{p}}}{\partial z^2}. \tag{4}$$

By combining Eqs. (3) and (4), we can get a combined conservation of momentum by eliminating the fluid stress tensor T_{f}

$$\begin{aligned} &(1-\varepsilon)\varepsilon \rho_{\mathrm{p}} \left(\frac{\partial u_{\mathrm{p}}}{\partial t} + u_{\mathrm{p}} \frac{\partial u_{\mathrm{p}}}{\partial z} \right) - (1-\varepsilon)\varepsilon \rho_{\mathrm{f}} \left(\frac{\partial u_{\mathrm{f}}}{\partial t} + u_{\mathrm{f}} \frac{\partial u_{\mathrm{f}}}{\partial z} \right) \\ &\quad = F_{\mathrm{I}} - [\varepsilon (1-\varepsilon)(\rho_{\mathrm{p}} - \rho_{\mathrm{f}}) g] + \varepsilon E_{\mathrm{p}} \frac{\partial \varepsilon}{\partial z} + \varepsilon \eta_{\mathrm{p}} \frac{\partial^2 u_{\mathrm{p}}}{\partial z^2}. \end{aligned} \tag{5}$$

Here the z-direction is chosen to be opposite to the direction of gravity. The symbols E_{p} represent the particle phase effective elasticity, η_{p} represents the particles phase effective viscosity, and F_{I} is the phase interacting force in z-direction. When linearized and formulated in one-dimension, nearly all models of multiphase flows fall into these forms (although in some models, some of the coefficients would be zero). The one exception is the model of Zhang and Prosperetti (1994) which permits a dependence on higher-order gradients of the fluid pressure – a term which is insignificant unless there are large changes in the fluid gradient within a particle diameter and thus may be significant only for large particles.

2.2.4. Generic stability analysis of homogeneous fluidization

Let $\varepsilon_0, u_{\mathrm{f0}}, u_{\mathrm{p0}}, F_{\mathrm{I0}}$ be the void fraction, velocities and the interaction force that correspond to a state of uniform fluidization, and u_0 be the superficial fluid velocity. Under those conditions: $\varepsilon_0 = \text{const},\ u_{\mathrm{f0}} = u_0/\varepsilon_0,\ u_{\mathrm{p0}} = 0$. Let the flow then be disturbed by $\varepsilon', u'_{\mathrm{f}}, u'_{\mathrm{p}}, F'_{\mathrm{I}}$, i.e

$$\varepsilon = \varepsilon_0 + \varepsilon',$$

$$u_\mathrm{f} = u_{\mathrm{f}0} + u'_\mathrm{f},$$

$$u_\mathrm{p} = u_{\mathrm{p}0} + u'_\mathrm{p},$$

$$F_\mathrm{I} = F_{\mathrm{I}0} + F'_\mathrm{I}.$$

Assuming that the phase interaction consists of drag and added mass forces

$$F_\mathrm{I} = F_\mathrm{d}(\varepsilon, u_\mathrm{f} - u_\mathrm{p}) + \theta(\varepsilon)\rho_\mathrm{f}\frac{\mathrm{d}_\mathrm{p}}{\mathrm{d}t}(u_\mathrm{f} - u_\mathrm{p}) \tag{6}$$

and

$$F'_\mathrm{I} = \alpha\frac{F_{\mathrm{d}0}}{u_{\mathrm{f}0}}(u'_\mathrm{f} - u'_\mathrm{p}) - \beta\frac{F_{\mathrm{d}0}}{\varepsilon_0}\varepsilon' + \theta_0\rho_\mathrm{f}\frac{\mathrm{d}_\mathrm{p}}{\mathrm{d}t}(u'_\mathrm{f} - u'_\mathrm{p}). \tag{7}$$

Here F_d is the drag force and the second term in Eq. (6) represents the added mass effect. In Eq. (7)

$$\alpha = \frac{u_{\mathrm{f}0}}{F_{\mathrm{d}0}}\frac{\partial F_\mathrm{d}}{\partial(u_\mathrm{f} - u_\mathrm{p})}$$

is the frag slope vs slip velocity,

$$\beta = -\frac{\varepsilon_0}{F_{\mathrm{d}0}}\frac{\partial F_\mathrm{d}}{\partial\varepsilon}$$

is the drag slope vs voidage and θ_0 is the added mass coefficient $(= \theta(\varepsilon_0))$. Note: originally we excluded the added mass effects from the generic model, but found that the values we obtained for the drag slopes were not comparable in magnitude with those in existing models. That meant that the common models were either very wrong or that the generic model was incomplete in some way. The only physically meaningful term to include was the added mass effect and its addition gave us drag slopes that were comparable in magnitude to common models.) The $\mathrm{d}_\mathrm{p}/\mathrm{d}t$ is the material time derivative of the particle phase

$$\frac{\mathrm{d}_\mathrm{p}}{\mathrm{d}t} = \frac{\partial}{\partial t} + U_\mathrm{p}\frac{\partial}{\partial x}.$$

Note that there are two other alternative forms of the material derivative proposed by Homsy et al. (1980) and Anderson and Jackson (1968a). The difference arises because the velocity of the convective term can be any one of: $u_\mathrm{p}, u_\mathrm{f}, u_\mathrm{f} - u_\mathrm{p}$. We feel that, as this term represents the effect of particle acceleration on the total force of the particle phase, the particle phase velocity should be the most appropriate choice for the convective term.

Now under uniform state conditions:

$$u_{\mathrm{p}0} = 0,$$

$$F_{\mathrm{I}0} = F_{\mathrm{d}0} = \varepsilon_0(1 - \varepsilon_0)(\rho_\mathrm{p} - \rho_\mathrm{f})g$$

and eliminating u'_f and u'_p, we get

$$A\frac{\partial^2\varepsilon'}{\partial t^2}+B\frac{\partial^2\varepsilon'}{\partial z\,\partial t}+C\frac{\partial^2\varepsilon'}{\partial z^2}+F\frac{\partial\varepsilon'}{\partial t}+G\frac{\partial\varepsilon'}{\partial z}=E\frac{\partial^3\varepsilon'}{\partial z^2\,\partial t}, \tag{8}$$

where

$$A=\rho_p\varepsilon_0+\rho_f(1-\varepsilon_0)+\frac{\rho_f}{\varepsilon_0(1-\varepsilon_0)}\theta_0,$$
$$B=2\rho_f(1-\varepsilon_0)u_{f0}+2\rho_f\frac{u_{f0}}{\varepsilon_0}\theta_0,$$
$$C=\rho_f(1-\varepsilon_0)u_{f0}^2-\varepsilon_0E_{p0},$$
$$F=\alpha\frac{F_{d0}}{u_{f0}}\frac{1}{\varepsilon_0(1-\varepsilon_0)},$$
$$G=\alpha\frac{F_{d0}}{\varepsilon_0}+\beta\frac{F_{d0}}{\varepsilon_0}+(1-2\varepsilon_0)(\rho_p-\rho_f)g,$$
$$E=\frac{\varepsilon_0\eta_{p0}}{1-\varepsilon_0}.$$

Eq. (8) can be used to describe linear instabilities in uniformly fluidized beds. Please note here that all of the coefficients in Eq. (8) are determined by five parameters: the drag-slope (α,β), the effective elasticity (E_{p0}), the effective viscosity (η_{p0}) and the added mass coefficient (θ_0). Most of other instability models give a similar equation although terms may be missing due to variances in the assumed constitutive models (Liu, 1982).

2.2.5. The inverse instability problem

Based on early experimental studies on the instability waves (Anderson and Jackson, 1968b; El-Kaissy and Homsy, 1976), it is clear that the waves are growing in the spatial domain rather than in the temporal domain. Although these spatial and temporal growthrates are related simply by the wavespeed of the instability waves, it will be much more realistic to directly use a spatially growing wave formula. So in this section and afterwards we will adopt spatially growing small disturbance formula: $\varepsilon'=e^{\sigma z+i(\omega t-kz)}=e^{i\omega t}e^{z(\sigma-ki)}$.

Applying this to Eq. (8), we get

$$A(-\omega^2+B(k\omega+\sigma\omega i)+C(\sigma^2-k^2-2\sigma ki)+F(i\omega)+G(\sigma-ik)=E(i\omega(\sigma^2-k^2)+2\sigma\omega k),$$

which has a real part

$$A(-\omega^2)+Bk\omega+C(\sigma^2-k^2)+G\sigma=E2\sigma\omega k \tag{9}$$

and an imaginary part

$$B\sigma\omega-C2\sigma k+F\omega-Gk=E\omega(\sigma^2-k^2). \tag{10}$$

Here again, all of the coefficients (A,B,C,F,G,E) are functions of five unknown parameters $(\alpha,\beta,E_{p0},\eta_{p0}$ and $\theta_0)$ as in Eq. (8).

Rewriting (9) and (10) based on $\alpha,\beta,E_{p0},\eta_{p0}$ and θ_0 (the five unknowns), we get

Real part:

$$\alpha_1\alpha+\beta_1\beta+E_1E_{p0}+\eta_1\eta_{p0}+\theta_1\theta_0=R_1. \tag{11}$$

Imaginary part:

$$\alpha_2\alpha + \beta_2\beta + E_2E_{\mathrm{p}0} + \eta_2\eta_{\mathrm{p}0} + \theta_2\theta_0 = R_2, \tag{12}$$

where

$$\alpha_1 = \frac{F_{\mathrm{d}0}}{\varepsilon_0}\sigma,$$

$$\alpha_2 = \frac{F_{\mathrm{d}0}}{u_{\mathrm{f}0}}\left(\frac{\omega}{\varepsilon_0(1-\varepsilon_0)} - \frac{u_{\mathrm{f}0}}{\varepsilon_0}k\right),$$

$$\beta_1 = \frac{F_{\mathrm{d}0}}{\varepsilon_0}\sigma,$$

$$\beta_2 = -\frac{F_{\mathrm{d}0}}{\varepsilon_0}k,$$

$$E_1 = -\varepsilon_0(\sigma^2 - k^2),$$

$$E_2 = 2\varepsilon_0\sigma k,$$

$$\eta_1 = -\frac{2\varepsilon_0\sigma\omega k}{1-\varepsilon_0},$$

$$\eta_2 = -\frac{\varepsilon_0\omega(\sigma^2 - k^2)}{1-\varepsilon_0},$$

$$\theta_1 = 2\rho_{\mathrm{f}}\frac{u_{\mathrm{f}0}}{\varepsilon_0}k\omega - \frac{\rho_{\mathrm{f}}}{\varepsilon_0(1-\varepsilon_0)}\omega^2,$$

$$\theta_2 = 2\rho_{\mathrm{f}}\frac{u_{\mathrm{f}0}}{\varepsilon_0}\sigma\omega,$$

$$R_1 = (\rho_{\mathrm{p}}\varepsilon_0 + \rho_{\mathrm{f}}(1-\varepsilon_0))\omega^2 - 2\rho_{\mathrm{f}}(1-\varepsilon_0)u_{\mathrm{f}0}k\omega - \rho_{\mathrm{f}}(1-\varepsilon_0)u_{f_0}^2(\sigma^2 - k^2) - (1-2\varepsilon_0)(\rho_{\mathrm{p}} - \rho_{\mathrm{f}})g\sigma,$$

$$R_2 = -2\rho_{\mathrm{f}}(1-\varepsilon_0)u_{\mathrm{f}0}\sigma\omega + 2\rho_{\mathrm{f}}(1-\varepsilon_0)u_{\mathrm{f}0}^2\sigma k + (1-2\varepsilon_0)(\rho_{\mathrm{p}} - \rho_{\mathrm{f}})gk.$$

Here, it can be seen that all of the coefficients in Eqs. (11) and (12) are functions of the instability wave properties (ω, σ, U). Furthermore, each measured set of (ω, σ, U) will provide two equations: Eqs. (11) and (12). Thus, to solve for the five unknowns ($\alpha, \beta, E_{\mathrm{p}0}, \eta_{\mathrm{p}0}$ and θ_0), we need at least three sets of instability wave properties to get five equations for the five unknowns. In general, if we can experimentally measure N ($N \geqslant 3$) sets of instability wave properties: $[\omega_i, \sigma_i, U_i]$, $i = 1, \ldots, N$, then it is possible to form $2N$ linear systems of equations that may be solved for these five unknowns by applying a least-square error technique, i.e.

$$M = \begin{bmatrix} \alpha_{1i} & \beta_{1i} & E_1 & \eta_{1i} & \theta_{1i} \\ \alpha_{2i} & \beta_{2i} & E_{2i} & \eta_{2i} & \theta_{2i} \\ \vdots & \vdots & \vdots & \vdots & \vdots \\ \alpha_{1N} & \beta_{1N} & E_{1N} & \eta_{1N} & \theta_{1N} \\ \alpha_{2N} & \beta_{2N} & E_{2N} & \eta_{2N} & \theta_{2N} \end{bmatrix},$$

$$R = \begin{bmatrix} R_{1i} \\ R_{2i} \\ \vdots \\ R_{1N} \\ R_{2N} \end{bmatrix}, \qquad X = \begin{bmatrix} \alpha \\ \beta \\ E_{\mathrm{p0}} \\ \eta_{\mathrm{p0}} \\ \theta_0 \end{bmatrix}.$$

Then

$$X = M^{+}R, \tag{13}$$

where M^{+} is the pseudoinverse of matrix M.

Unfortunately, during this process, we discovered that the system equations for the inverse instability problem are ill conditioned and thus virtually unsolvable by any direct mathematical procedure. The ill conditioning was traced to the fact that the wavespeed did not vary greatly with the imposed frequency. To overcome this problem, an optimum parameter identification method was developed, whose accuracy is demonstrated by Jin (1996).

The optimum parameter identification method first reduces the condition number by reducing the rank of the matrix and keeping only two row vectors made of coefficients from two different equations (Eqs. (11) and (12)) in the matrix. This reduces the number of linear equations to two, which can be solved for only two of the unknown parameters. The other three parameters are determined by a best fit technique. To do this, three "fitting" parameters are chosen and varied through all physically acceptable values, all the time solving the matrix equation for the other two parameters until the best fit to the experimental data is achieved.

The three fitting parameters are α, β and θ_0. They are chosen such that we can limit the range of possible values based on exciting theory or empirical data.

For example the α must lie between (Jin, 1996)

$$\alpha_{\max} = 1 + \frac{0.63\sqrt{Re_{\mathrm{t}}}}{4.90 + 0.63\sqrt{Re_{\mathrm{t}}}}$$

and

$$\alpha_{\min} = 1 + \frac{0.63\sqrt{Re_{\mathrm{mf}}}}{4.90 + 0.63\sqrt{Re_{\mathrm{mf}}}},$$

where $Re_{\mathrm{t}} = u_{\mathrm{t}} d_{\mathrm{p}} \rho_{\mathrm{f}} / \mu_{\mathrm{f}}$ is terminal Reynolds number (u_{t} is terminal velocity), and $Re_{\mathrm{mf}} = u_{\mathrm{mf}} d_{\mathrm{p}} \rho_{\mathrm{f}} / \mu_{\mathrm{f}}$ is Reynolds number corresponding to the minimum fluidization velocity (where u_{mf} is the minimum fluidization velocity) and β ranged from 0 to 5; and the θ_0 ranged from 0 and 20 (see the detailed discussion in Jin, 1996).

The optimum parameter identification procedure can be summarized as follows: We start with the measured wave properties, and a set of estimated fitting parameters $X_0 = [\alpha\ \beta\ \theta_0]^{\mathrm{T}}$ in the ranges described above. From that, we solve for the remaining values of $X_{\mathrm{s}} = [E_{\mathrm{p0}}\ \eta_{\mathrm{p0}}]^{\mathrm{T}}$ from Eq. (13), yielding a complete set of estimated solutions, $[\alpha\ \beta E_{\mathrm{p0}}\ \eta_{\mathrm{p0}}\ \theta_0]^{\mathrm{T}}$. From those, using Eqs. (9) and (10), predictions are made of the growthrate and wavespeed for each frequency which can be compared against the experimentally measured values. The optimum choices of, $[\alpha\ \beta E_{\mathrm{p0}}\ \eta_{\mathrm{p0}}\ \theta_0]^{\mathrm{T}}$ are those that minimize the mean square difference between the predicted and measured wave properties.

3. Constitutive parameters and comparison with other models

Based on these experimental wave properties given in the previous section, the system parameters ($\alpha, \beta, E_p, \eta_p$, and θ) for the three different particle sizes at various voidages can be determined by the optimum parameter identification method. An error bar sits on each point which was calculated by applying estimated maximum errors to the measured values. For example 10% error was applied to the growthrate based on the range for which reasonable linear curve fits could be made to the data. A 2% error in wavespeed which was based on the maximum scatter in the wavespeed data in the linear growth region. (The wavespeed measurements were very stable.) No error has been applied to forced wave frequencies as the frequency measured was always exactly same as the forced frequency, but 1% error in frequencies for supplemental growthrate measurements has been applied based on the width of the notch filter used to collect this data. The error on the mean voidage is based on the bed height fluctuation during the measurements at the mean voidage conditions, which was 0.2% for set A, 0.3% for set B and set C.

3.1. Drag slopes

The derivatives of the drag forces versus slip velocity, α, are presented in Figs. 2–4, and the derivatives of the drag force versus void fraction, β are presented in Figs. 5–7. A comparison has been made with the three most popular drag models: the Ergun model (Ergun, 1952), the Richardson and Zaki model (Richardson and Zaki, 1954) and the Foscolo–Gibilaro model (Foscolo and Gibilaro, 1984, 1987). The Ergun and Richardson–Zaki models are summarized in Shook and Roco (1991) as

Ergun:

$$F_{erg} = \left[1.75 + \frac{150\mu_f(1-\varepsilon)}{d_p\rho_f(u_f - u_p)\varepsilon}\right]\frac{\rho_f(u_f - u_p)^2(1-\varepsilon)}{d_p}. \tag{14}$$

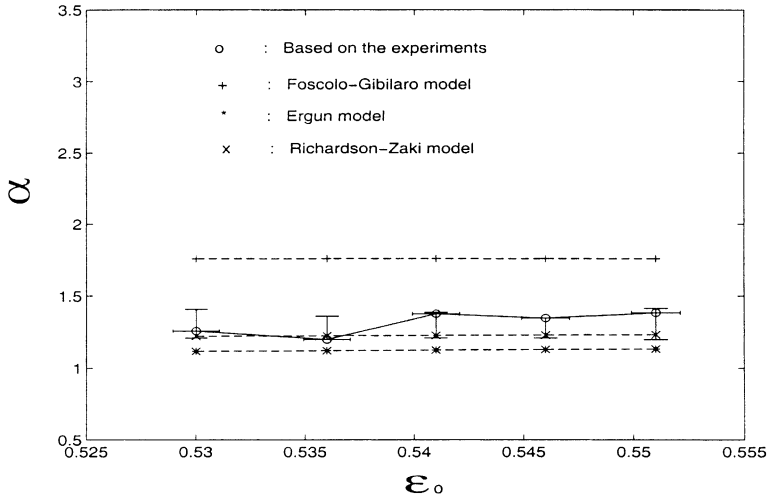

Fig. 2. Drag derivative vs slip velocity for set A.

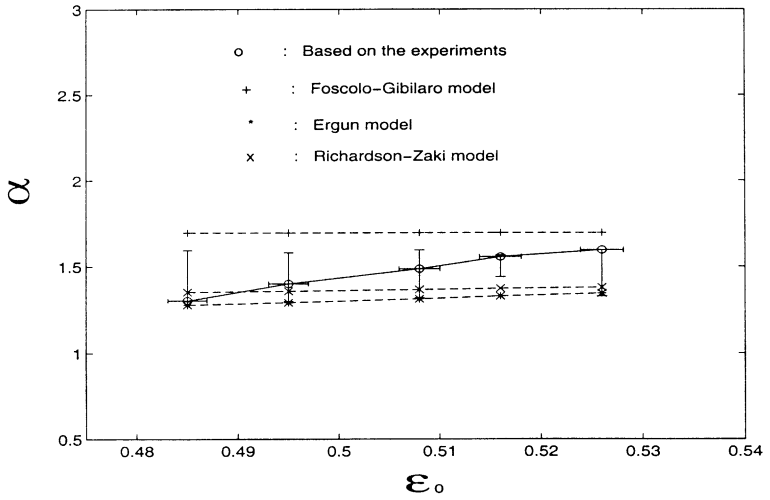

Fig. 3. Drag derivative vs slip velocity for set B.

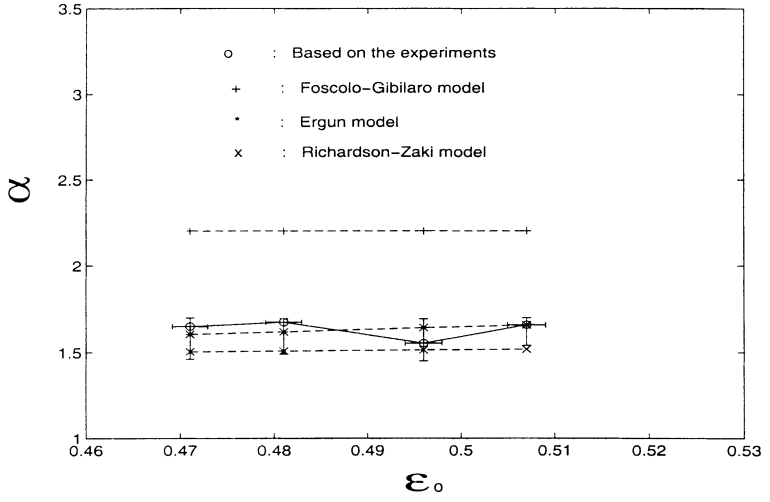

Fig. 4. Drag derivative vs slip velocity for set C.

Thus

$$\alpha_{\mathrm{erg}} = \frac{u_{\mathrm{f0}}}{F_{\mathrm{erg0}}}\left[\frac{\partial F_{\mathrm{erg}}}{\partial(u_{\mathrm{f}} - u_{\mathrm{p}})}\right]_{\varepsilon=\varepsilon_0} = \frac{u_{\mathrm{f0}}}{F_{\mathrm{erg0}}}\frac{\rho_{\mathrm{f}}}{d_{\mathrm{p}}}\left[3.5u_{\mathrm{f0}} + \frac{150\mu_{\mathrm{f}}(1-\varepsilon_0)}{\rho_{\mathrm{f}} d_{\mathrm{p}}\varepsilon_0}\right](1-\varepsilon_0) \tag{15}$$

and

$$\beta_{\mathrm{erg}} = -\frac{\varepsilon_0}{F_{\mathrm{erg0}}}\left[\frac{\partial F_{\mathrm{erg}}}{\partial \varepsilon}\right]_{\varepsilon=\varepsilon_0} = \frac{\varepsilon_0}{F_{\mathrm{erg0}}}\left[1.75\frac{\rho \partial_{\mathrm{f}} u_{\mathrm{f0}}^2}{d_{\mathrm{p}}} + \frac{150\mu_{\mathrm{f}} u_{\mathrm{f0}}(1-\varepsilon_0^2)}{d_{\mathrm{p}}^2\varepsilon_0^2}\right], \tag{16}$$

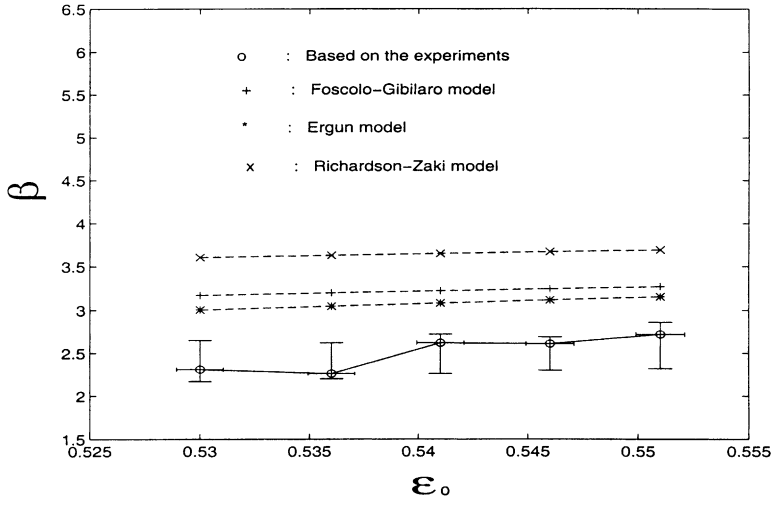

Fig. 5. Drag derivative vs voidage for set A.

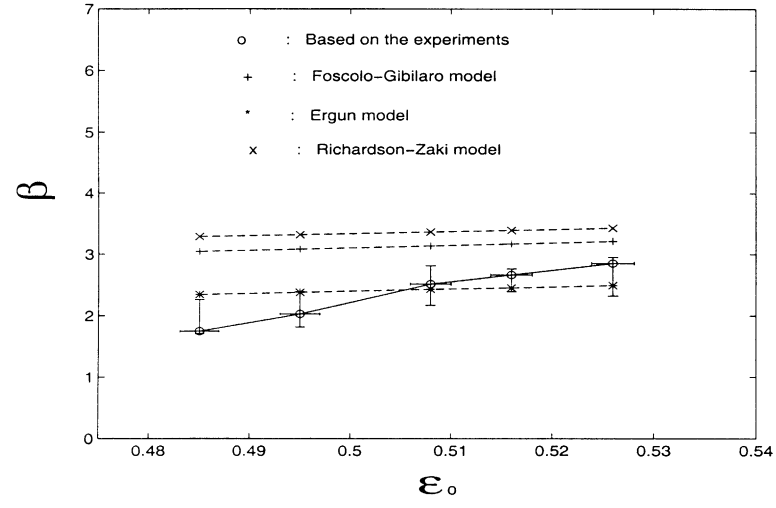

Fig. 6. Drag derivative vs voidage for set B.

where

$$F_{\mathrm{erg0}} = \left[1.75 + \frac{150\mu_{\mathrm{f}}(1-\varepsilon_0)}{d_{\mathrm{p}}\rho_{\mathrm{f}}u_{\mathrm{f0}}\varepsilon_0}\right]\frac{\rho_{\mathrm{f}}u_{\mathrm{f0}}^2(1-\varepsilon_0)}{d_{\mathrm{p}}}.$$

The Richardson–Zaki model (as generalized by Wallis, 1969)

$$F_{\mathrm{rz}} = \frac{3C_{\mathrm{Ds}}(1-\varepsilon)\rho_{\mathrm{f}}(u_{\mathrm{f}}-u_{\mathrm{p}})^2}{4d_{\mathrm{p}}\varepsilon^{1.7}}, \tag{17}$$

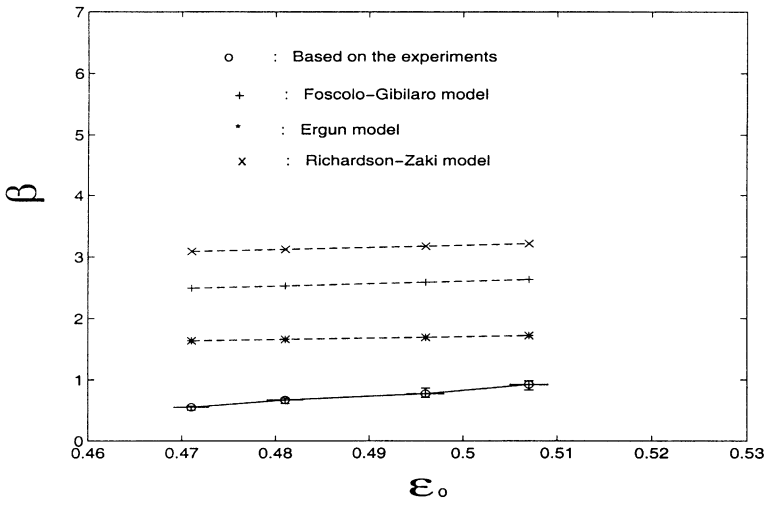

Fig. 7. Drag derivative vs voidage for set C.

so

$$\alpha_{\mathrm{rz}} = \frac{u_{\mathrm{f0}}}{F_{\mathrm{erg0}}}\left[\frac{\partial F_{\mathrm{erg}}}{\partial(u_{\mathrm{f}}-u_{\mathrm{p}})}\right]_{\varepsilon=\varepsilon_0} = 2 + \frac{u_{\mathrm{f0}}}{C_{\mathrm{Ds0}}}\left[\frac{\partial C_{\mathrm{Ds}}}{\partial(u_{\mathrm{f}}-u_{\mathrm{p}})}\right]_{\varepsilon=\varepsilon_0} \tag{18}$$

and

$$\beta_{\mathrm{rz}} = -\frac{\varepsilon_0}{F_{\mathrm{rz0}}}\left[\frac{\partial F_{\mathrm{rz}}}{\partial \varepsilon}\right]_{\varepsilon=\varepsilon_0} = \frac{1.7-0.7\varepsilon_0}{1-\varepsilon_0} - \frac{\varepsilon_0}{C_{\mathrm{Ds0}}}\left[\frac{\partial C_{\mathrm{Ds}}}{\partial \varepsilon}\right]_{\varepsilon=\varepsilon_0}, \tag{19}$$

where

$$F_{\mathrm{rz0}} = \frac{3C_{\mathrm{Ds0}}(1-\varepsilon_0)\rho_{\mathrm{f}}u_{\mathrm{f0}}^2}{4d_{\mathrm{p}}\varepsilon^{1.7}}$$

and

$$C_{\mathrm{Ds}} = \frac{24}{Re_{\mathrm{s}}} \quad \text{for } Re_{\mathrm{s}} = \frac{\varepsilon d_{\mathrm{p}}(u_{\mathrm{f}}-u_{\mathrm{p}})\rho_{\mathrm{f}}}{\mu_{\mathrm{f}}} < 0.2,$$

$$C_{\mathrm{Ds}} = \frac{24}{Re_{\mathrm{s}}}(1+0.15Re_{\mathrm{s}}^{0.687}) \quad \text{for } 0.2 < Re_{\mathrm{s}} < 1000,$$

$$C_{\mathrm{Ds}} = 0.44 \quad \text{for } Re_{\mathrm{s}} > 1000.$$

From Foscolo and Gibilaro (1984, 1987)

$$F_{\mathrm{fg}}(\varepsilon, u_{\mathrm{f}}-u_{\mathrm{p}}) = (1-\varepsilon)\varepsilon^{(4.8-3.8n)/n}(\rho_{\mathrm{p}}-\rho_{\mathrm{f}})g\left(\frac{u_{\mathrm{f}}-u_{\mathrm{p}}}{u_t}\right)^{4.8} n, \tag{20}$$

so

$$\alpha_{\mathrm{fg}} = \frac{u_{\mathrm{f0}}}{F_{\mathrm{fg0}}}\left[\frac{\partial F_{\mathrm{fg}}}{\partial(u_{\mathrm{f}} - u_{\mathrm{p}})}\right]_{\varepsilon=\varepsilon_0} = \frac{4.8}{n} \tag{21}$$

and

$$\beta_{\mathrm{fg}} = \frac{\varepsilon_0}{F_{\mathrm{fg0}}}\left[\frac{\partial F_{\mathrm{fg}}}{\partial \varepsilon}\right]_{\varepsilon=\varepsilon_0} = \frac{3.8 - 2.8\varepsilon_0}{1 - \varepsilon_0} - \frac{4.8}{n}. \tag{22}$$

Here, the terminal velocity and the exponent n are found from measurements of bed expansion for the various materials used in this study.

Fig. 2 presents the void velocity derivative α for set A (0.5 mm) which is the smallest size tested in this study. The measurements covered a voidage range from 0.530 to 0.55 and the variations of α in this range are small. The Richardson–Zaki model makes the most accurate predictions, while Ergun's model predicted slightly smaller values than the experiments. But on the opposite side, the Foscolo–Gibilaro model overpredicts the experiments. Fig. 3 presents the α for set B (1.0 mm) which is the intermediate size tested. The mean voidage ranges from 0.48 to 0.53.

For set B (1 mm beads), a slightly larger variation is observed and α shows an almost linear increase with voidage. Here, most of the data points lie between the Foscolo–Gibilaro and the Richardson–Zaki models, and, again, Ergun's model again predicts lower values than the measurements. Fig. 4 presents the velocity derivative α for set C (2.0 mm) which is the largest size tested with the voidage ranging from 0.47 to 0.51. Here the Ergun model give very reasonable accuracy, while the predictions of the Richardson–Zaki model are slightly lower than the experiments, while the Foscolo–Gibilaro model predicted much larger values. The data points show a clear increasing trend as the voidage is increased.

Fig. 5 shows the voidage derivative β for set A. The results show that all of the models predicted higher values than the experiments; the Ergun model does the best job but still overpredicts the data by about 15%. As for the corresponding values for α, there is little variation with voidage. Fig. 6 shows the derivative β for set B. The Ergun model still gives reasonable agreement, and the other two models are again higher than the measurements. Fig. 7 shows the derivative β for set C. Here, all of the models predict much higher values than the experiments for set C. The value β generally increases with increasing voidage.

A tremendous discrepancy between the measured and predicted values of β is observed especially for the largest glass beads. This suggests that the discrepancy might be partially due to finite size effects (i.e. that the particle size is a significant fraction of the wavelength, i.e. here $d_{\mathrm{p}} = 2.0$ mm and wavelength $\lambda \sim 20$ mm, so $d_{\mathrm{p}}/\lambda \sim 0.1$). One correction for finite particle sizes has been proposed by Singh and Joseph (1995). This method was incorporated into our instability analysis, but unfortunately, the resulting correction was much too small to account for the observed discrepancy (although the correction does lie in the right direction). Nevertheless the idea of considering finite particle size in the particle motion equation does still appear to hold merit. Based on the set C data, the voidage within a wave does vary significantly over a particle size. This means that continuum theory which assumes that all physical variables change in a length scale much larger than particle diameter may well break down for these beads. Some of these physics are captured in the higher-order pressure term that appears in the theory of Zhang and Prosperetti (1994), which will become important if the pressure gradient varies significantly over a particle diameter.

At least in the context of these instability analyses, the results indicate that none of these drag models should be used for instability analyses of large beads without suitable modification.

3.2. Particle effective elasticity

The particle phase effective elasticities are shown in Figs. 8–10. Comparison has been made with the Foscolo–Gibilaro model (Foscolo and Gibilaro, 1984, 1987) as it is the only model available. The Foscolo–Gibilaro elasticity model predicts

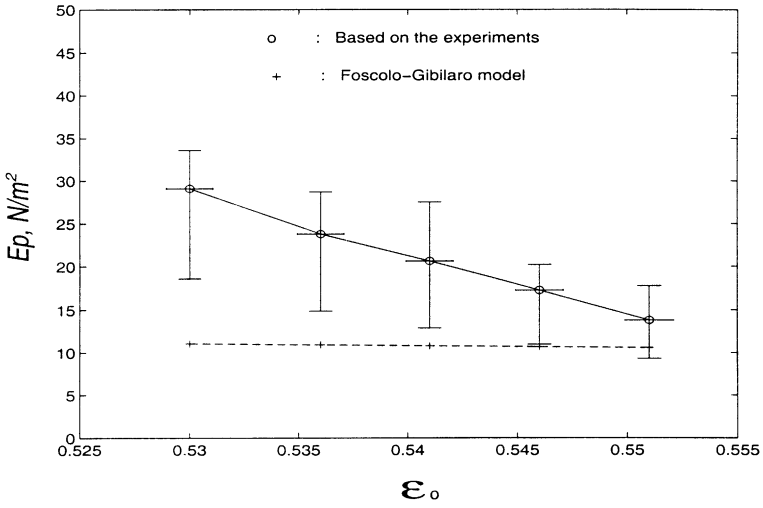

Fig. 8. Particulate effective elasticity for set A.

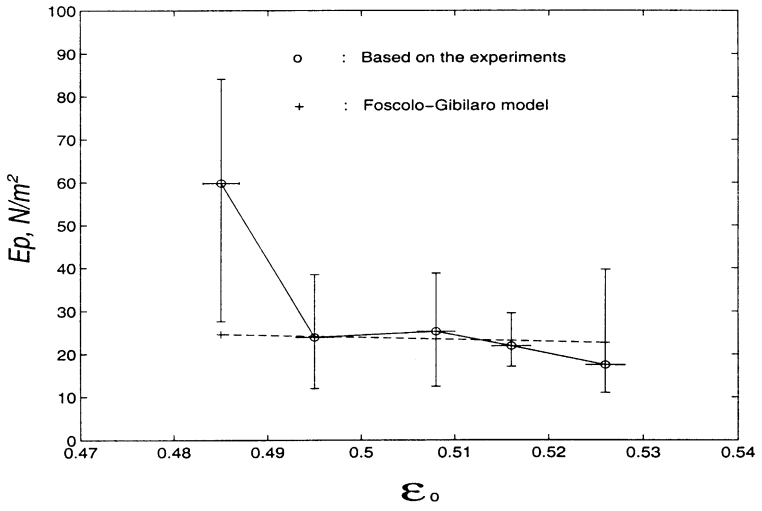

Fig. 9. Particulate effective elasticity for set B.

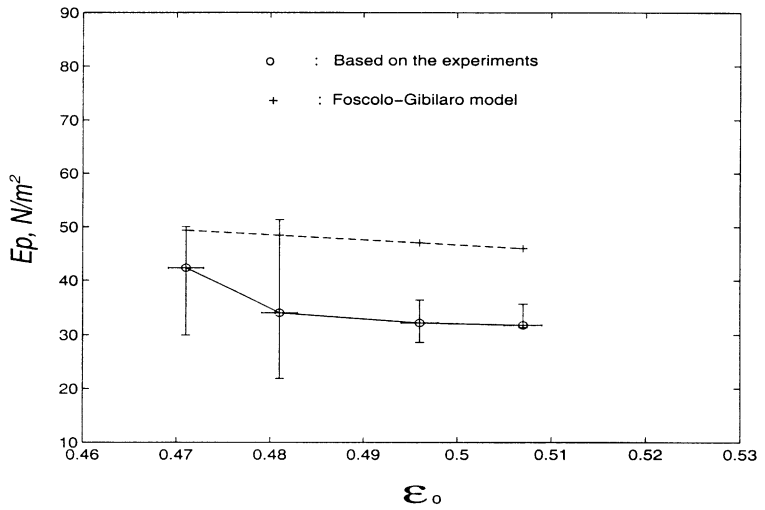

Fig. 10. Particulate effective elasticity for set C.

$$E_{\mathrm{pfg}} = 3.2 g d_{\mathrm{p}} (1-\varepsilon)(\rho_{\mathrm{p}} - \rho_{\mathrm{f}}). \tag{23}$$

Fig. 8 shows measurements of particulate effective elasticity for set A ((0.5 mm). The Foscolo–Gibilaro model predicts lower values than the measurements. The data also show a clear decreasing (almost linearly decreasing) trend as the voidage is increased which is also not apparent in the Foscolo–Gibilaro model. (Note that as the Foscolo–Gibilaro model varies as $(1-\varepsilon)$, it will show very little voidage variation within the small range of voidages for which linear wave growth may be experimentally observed.) Fig. 9 shows particulate effective elasticities for set B (1.0 mm). For most of the data points, the Foscolo–Gibilaro model gives reasonable agreement except for the one point at the lowest voidage. The measured data again decreases more rapidly than the Foscolo–Gibilaro model. Fig. 10 shows the results for set C (2.0 mm). Here the Foscolo–Gibilaro model gives higher values than the experiments, but both the models and measured data decrease with approximately same slope as the voidage increases except at the lower voidage. Note that the particulate effective elasticity predicted by the Foscolo–Gibilaro model is proportional to the particle diameter, but the data show very little dependence on particle size.

3.3. Particulate effective viscosity

The particulate phase effective viscosities are shown in Figs. 11–13. No comparison with theory is available for this parameter other than for the viscosity of suspensions (which are much smaller than any of these measurements and are thus not shown). However, one would expect there to be a strong voidage effect on the results as the viscosity should be effectively infinite at small voidages when the particles interlock and the material exhibits a solid-like behavior. One would also expect the viscosity to decrease rapidly with voidage from that point on.

Fig. 11 presents the particulate effective viscosities for set A. The results show that the effective viscosities are in the range of 1–3 poise, and decrease modestly with increasing voidage. This small voidage change may be due to the relatively large voidages for which linearly growing waves are

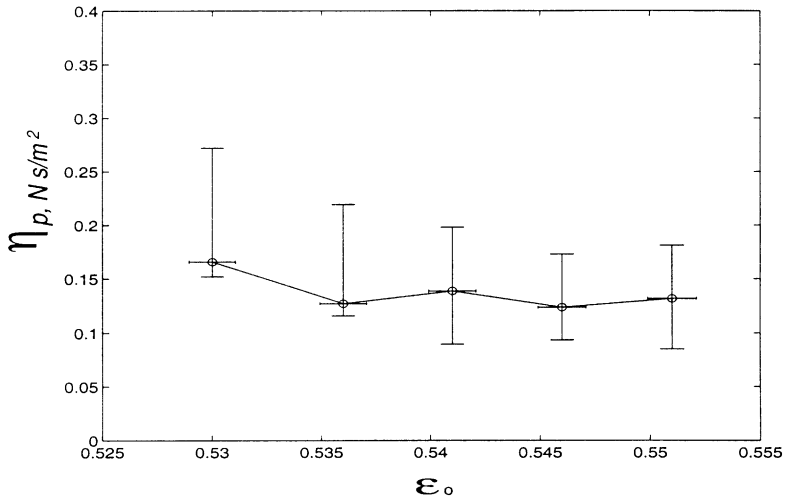

Fig. 11. Particulate effective viscosity for set A.

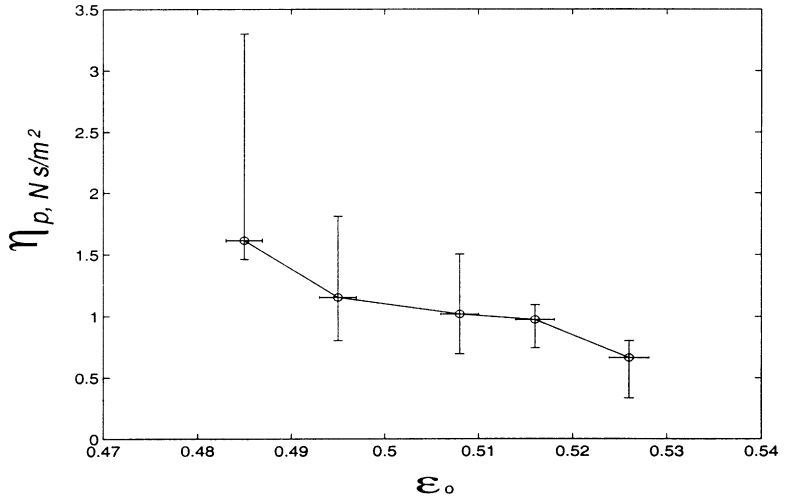

Fig. 12. Particulate effective viscosity for set B.

discernable for these small particles. Fig. 12 shows the results for set B. The effective viscosities for set B ranges from 5 to 25 poise and also decrease with increasing voidage. Fig. 13 shows the results for set C which lie in the same range, but decrease more rapidly with increasing voltage.

Based on the results of sets A and B, the particulate effective viscosity seems to increase with increasing particle diameter, but the results of sets B and C lie roughly in the same range. This indicates that the particulate effective viscosity is sensitive to particle diameter for small beads, but does not appear for large beads ($d_p > 1$ mm in this case). Here we should particularly note that the voidage ranges for three different beads sizes are different. The larger the bead size, the lower the voidage range available before the growth of the instabilities rapidly become nonlinear and

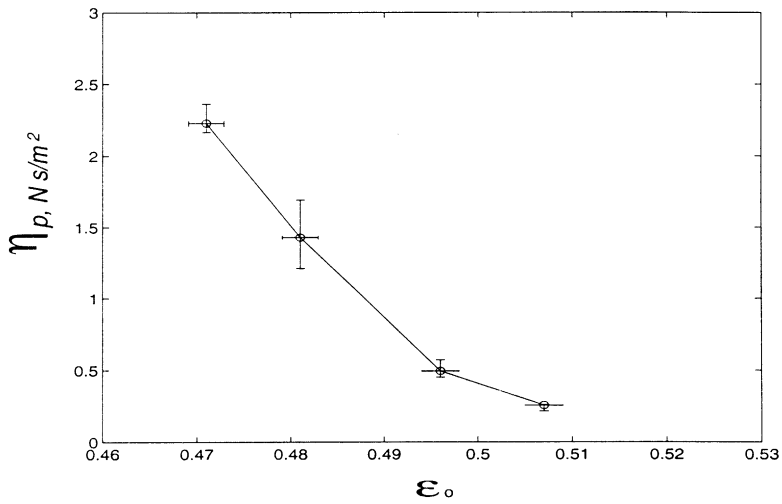

Fig. 13. Particulate effective viscosity for set C.

chaotic. All of the data prove that the particulate effective viscosity decreases with increasing voidage and the effective viscosity for the larger beads appear to decrease more rapidly.

The results presented here are approximately in the same order as those measured by Schügerl et al. (1961) in a concentric cylinder viscometer which contained a gas-fluidized bed, and as inferred from the motion of bubbles by Grace (1970), also in a gas-fluidized bed. To our knowledge, the current measurements are the first such determinations made in liquid-fluidized beds. This may provide some insight into the mechanism of viscosity generation. If one were to assume that the values should scale with the viscosity of the interstitial fluid, (as one would expect for a suspension), then the relative viscosities, η_p/μ_f measured here are off by orders of magnitude from their corresponding values for gas-fluidized beds. However, if one assumes that these viscosities are primarily a result of momentum transport induced by particle motion and interactions, the values should be relatively independent of the fluid; in that case, the results in gas and liquid-fluidized beds should be similar just as observed in these results. This outcome was also predicted by Anderson and Jackson (1968a).

3.4. Added mass effects

Figs. 14–16 show the results for the added mass coefficients. The values range from about 2 to slightly less than 14 and decrease with increasing voidage for all cases. The larger beads tend to have stronger dependence on the voidage than the smaller beads, but again, this might be a result of the different range of voidages for which linear waves are apparent. These values are roughly in line with the values estimated by Homsy et al. (1980). There are no other quantitative values available for comparison although there are some theoretical analyses of the added mass effect (Geurst, 1991; Drew et al., 1979).

These are probably the most controversial results in this paper even though they are in line with the Homsy et al. measurements. The biggest concern is that these values are so much larger than

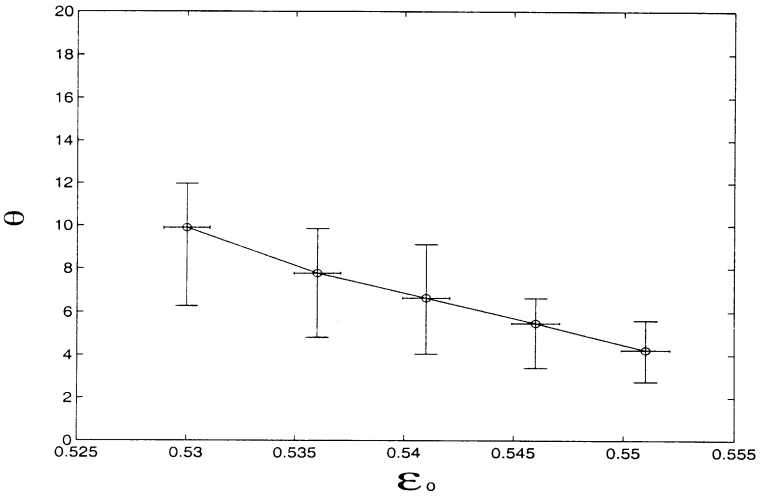

Fig. 14. Added mass coefficient for set A.

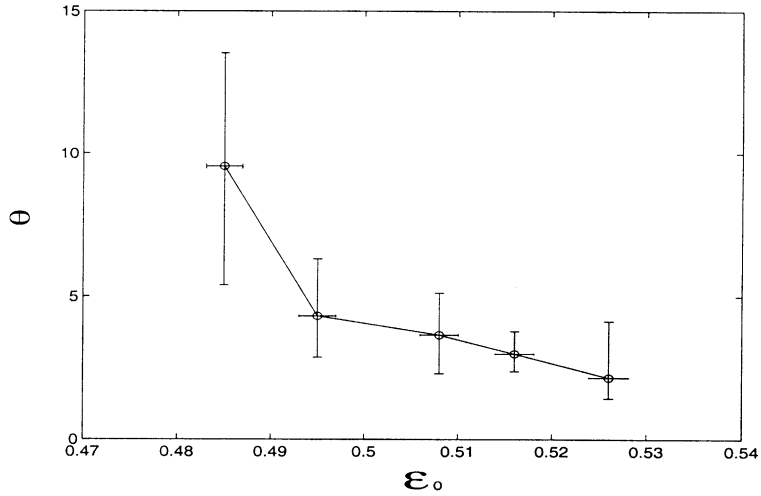

Fig. 15. Added mass coefficient for set B.

theoretical predictions, that it is not practicable to present the theoretical results on the plots. But in addition, the added mass coefficient is itself a somewhat controversial concept in multiphase flows. Many studies state that the added mass coefficient should be in the range of 0–0.5 (Atkinson and Kytomaa, 1992; Dodemand et al., 1995), with the value increasing with voidage and assuming the value of 0.5 when the voidage goes to unity (simply because 0.5 is the value for a single sphere in an infinite fluid). Other analyses, Felderhof (1991), Sangani et al. (1991) and Zhang and Prosperetti (1994), predict the opposite behavior, that the added mass will decrease with voidage. Similarly, Guo and Chwang (1992) have analyzed the added mass tensor for two spheres and also obtain component values slightly larger than 0.5 that increase as the spheres approach each other and go to 0.5 as the spheres separate. The analyses of Felderhof (1991), Sangani et al. (1991) and

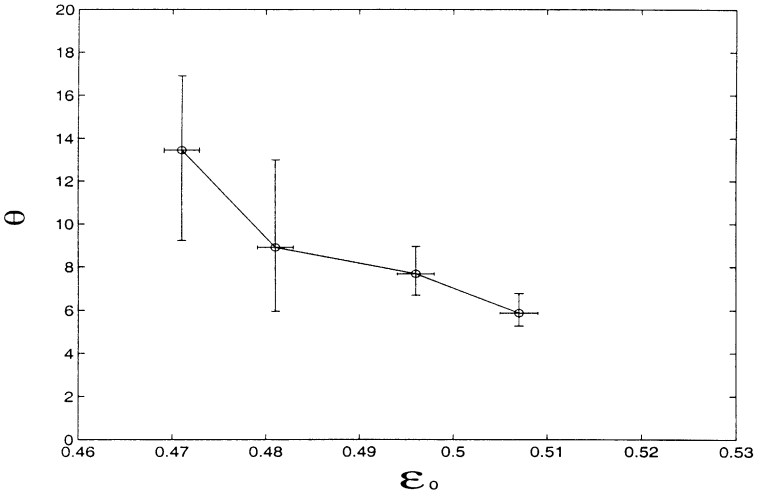

Fig. 16. Added mass coefficient for set C.

Zhang and Prosperetti (1994), incorporate the complete physics and predict the same general trends, if smaller values for the added mass coefficients than are seen here.

4. Conclusions

This paper has presented constitutive measurements for the various properties that appear in interpenetrating continuum stability models for fluidized beds. First, an inverse model was created starting with a generic stability model (one with all constitutive parameters left undetermined). The next step was to perform experimental measurements of the linear growth of forced instability waves in liquid-fluidized beds. The original intention was to perform the inverse problem to determine the values of the constitutive parameters, but the direct inverse problem proved to be ill conditioned, largely because the instability wavespeed did not vary greatly from case to case. As a result, the inverse problem had to be performed using an Optimum Parameter Identification Method, which provides answers that are less precise than a well-conditioned direct inversion, but is still able to yield sufficiently precise values to distinguish between many proposed models. This technique yields values for the parameters that appear directly in the instability models: the derivatives of the drag law with respect to voidage and velocity, the effective elasticity, viscosity and the added mass coefficient. Collectively these encompass virtually all of the instability models that have been so far proposed.

Perhaps the most important use of this data is to evaluate the various drag laws that are common in the literature. Note that this technique does not directly evaluate drag models only their derivatives with respect to voidage and velocity. In general, the Ergun and Richardson–Zaki models did the best job of predicting the data while the Foscolo–Gibilaro model generally overpredicted the results. Interestingly, all the models generally overpredicted the drag derivative with respect to voidage. Finally, there was some evidence of finite size effects appearing for the

largest particles studied when the particle size begins to become comparable to the wavelength of the instability.

The effective elasticity of the bed is a particularly important quantity for fluidized bed instabilities as it reflects the direct resistance applied by the bed to voidage growth and thus reflects the internal mechanisms that stabilize both liquid-fluidized beds and gas-fluidized beds of fine particles. In general, the elasticity decreased with an increasing mean bed voidage. This is to be expected as the larger the voidage, the more unstable the bed. The value of the elasticity also generally increases with particle size. It is possible that the elasticity arises from either direct particle contacts, from a hydrodynamic source or some combination of the two. In these dense systems, one can imagine that there are long duration contacts between a particle and its neighbors that will elastically resist the bed expansion required to cause a local voidage increase. From a hydrodynamic point of view, the elasticity might be caused by a mechanism like the Bernoulli attraction between particles in a crossflow such as was studied by Kim et al. (1993a,b). Increasing the voidage (as is done by a passing instability wave) implies moving such particles apart and doing work against this force which would be experienced as an effective elasticity of the material.

The data indicate that the effective viscosity is most likely a result of direct particle interactions. Again, the argument is indirect but is apparent in the extremely large values found for the effective viscosity – much larger than obtained by rheological experiments on suspensions. Furthermore, the observed values drop dramatically as the voidage increases which is as one would expect since the number of particle interactions also drop dramatically with voidage for the high concentration systems studied here. Finally, the viscosity values are comparable to those measured by Schügerl et al. (1961) in gas-fluidized beds. That in itself indicates that the viscosities are nearly independent of the viscosity of the interstitial fluid. This last observation may be somewhat surprising if one were to imagine that the particle phase viscosity arises from interparticle collisions. If that were the case, then one might anticipate a stronger effect of the fluid viscosity than is observed here, since before two solid particles can collide, one must first drain away the intervening fluid layer which would be strongly resisted by viscous forces. However, the large concentrations where linear instabilities are observed are similar to those in the dense phase of a gas-fluidized bed (see for example the X-ray densitometry measurements of Yates et al., 1994) and it is likely that there may be enduring contacts between particles. Momentum transport along those contacts may well its appearance in the particle effective viscosity. (In fact, the particle pressure measurements of Campbell and Wang, 1991 and Rahman and Campbell, 2001, indicate that this is the mechanism of particle pressure transmission in bubbling gas-fluidized beds. In particular Rahman and Campbell, 2001 show that particle pressures are large in unagitated regions of the bed; as there is no agitation there is no apparent mechanism to support continuing particle collisions, leaving transmission over enduring contacts as the only possible explanation.)

Finally, the values of the added mass coefficients are very large much larger than predicted by any of the theories. Furthermore these measurements are quantitatively similar to those of Homsy et al. (1980), indicating that these values are somewhat robust. The authors are hesitant to make the simple judgement that the theoretical results are simply incorrect, but are more inclined to believe that there may be physics that are missing from the instability models of the types considered here. For example, if the situation discussed in the last paragraph proves to be true and that enduring contacts exist between particle, then it is not possible to accelerate a particle without

accelerating some of the particles with which it is intimate contact. In any case, the acceleration of a particle would certainly force contacts with its neighbors leading to much the same result. In other words, in a method analogous to the physics behind the added mass, these contacts extend the reach of the particle into the surrounding material, making it impossible to accelerate one particle without accelerating many of its neighbors. As a result, what appears as the added mass may include some of the surrounding particle mass in addition to that of the fluid. These physics are not included in any of the models mentioned here as that portion of the added mass would be completely independent of the fluid. Furthermore, this would not strictly be an added mass force as it occurs only the particle phase and not in the phase interaction forces. But, as the forces involve particle accelerations, they would most likely show up in the added mass coefficient. Thus much the same physics could explain the large magnitudes of both the effective viscosities and added mass coefficients.

Along the lines of the last paragraph, the reader is advised to take these results with some caution. Remember that these constitutive measurements are interpreted from an interpenetrating continuum stability model for fluidized beds. In other words, these are the values that best fit such models to the measured data. It is not clear that the values presented possess any validity outside that context. For example, it is not clear whether the viscosities determined here are applicable to other multiphase flow situations. In other words, these may well not be the viscosities that one would obtain in a Couette viscometer (although their similarities to the measurements of Schügerl et al., 1961 are encouraging). But, if the stability models that have appeared in the literature are accurate descriptions of the problem, then these results should be accurate representations of the constitutive properties.

Acknowledgements

This work was supported by the US Department of Energy under grant Grant # DE-FG03-91ER4223 for which the authors are very grateful.

References

Anderson, T.B., Jackson, R., 1968a. A fluid mechanical description of fluidized beds: stability of the state of uniform fluidization. Ind. Eng. Chem. Fundam. 7, 12–21.

Anderson, T.B., Jackson, R., 1968b. A fluid mechanical description of fluidized beds: stability of the state of uniform fluidization. Ind. Eng. Chem. Fundam. 8, 137–144.

Atkinson, C.M., Kytomaa, H.K., 1992. Acoustic wave speed and attenuation in suspensions. Int. J. Multiphase Flow 18, 577–592.

Batchelor, G.K., 1988. A new theory for the instability of a uniform fluidized bed. J. Fluid Mech. 193, 75–110.

Campbell, C.S., Wang, D.G, 1991. Particle pressure in gas-fluidized beds. J. Fluids Mech. 227, 495–508.

Clift, R., Grace, I.R., 1985. Continuous bubbling and slugging. In: Davidson, J.F., Clift, R., Harrision, D. (Eds.), Fluidization. Academic Press, London, pp. 73–128.

Dodemand, E., Prud'homme, R., Kuentzmann, P., 1995. Influence of unsteady forces acting on a particle in a suspension; Application to the sound propagation. Int. J. Multiphase Flow 21 (1), 27–51.

Drew, D.A., Cheng, L., Lahey Jr., R.T., 1979. The analysis of virtual mass effects in two-phase flow. Int. J. Multiphase Flow 5, 233–242.

El-Kaissy, M.M., Homsy, G.M., 1976. Instability waves and the origin of bubbles in fluidized beds. Int. J. Multiphase Flow 2, 379–395.
Ergun, S., 1952. Fluid flow through packed columns. Chem. Eng. Prog. 48 (2), 89–94.
Felderhof, B.U., 1991. Virtual mass and drag in two-phase flow. J. Fluid Mech. 225, 177–196.
Foscolo, P.V., Gibilaro, L.G., 1984. A fully predictive criterion for the transition between particulate and aggregate fluidization. Chem. Eng. Sci. 39 (12), 1667–1675.
Foscolo, P.V., Gibilaro, L.G., 1987. Fluid dynamic stability of fluidized suspensions. The particle bed model. Chem. Eng. Sci. 39, 1485–1500.
Geurst, J.A., 1991. Virtual mass and impulse of bubble dispersions: reply to a note by Van Wijngaarden. Int. J. Multiphase Flow 17, 815–821.
Grace, J.R., 1970. The viscosity of fluidized beds. Can. J. Chem. Eng. 48, 30–33.
Guo, Z., Chwang, A.T., 1992. On the planar translation of two bodies in a uniform flow. J. Ship Res. 36, 38–54.
Ham, J.M., Thomas, S., Guazzelli, E., Homsy, G.M., Anselmet, M.C., 1990. An experimental study of the stability of liquid-fluidized beds. Int. J. Multiphase Flow 16, 171–185.
Homsy, G.M., El-Kaissy, , Didawania, A., 1980. Instability waves and the origin of bubbles in fluidized beds, part II: comparison with theory. Int. J. Multiphase Flow 6, 305–318.
Jackson, R., 1985. Hydrodynamic stability of fliud-particle systems. In: Davidson, J.F., Clift, R., Harrision, D. (Eds.), Fluidization. Academic Press, London, pp. 47–72.
Jin, C., 1996. Generic stability model and experimental study of liquid-fluidized beds. Ph.D. Thesis, University of Southern California, Los Angeles, CA, USA.
Kim, I., Elghobashi, S., Sirignano, W.A., 1993a. Three-dimensional flow over two spheres placed side by side. J. Fluid Mech. 246, 465–488.
Kim, I., Elghobashi, S., Sirignano, W.A., 1993b. Three-dimensional flow over two spheres placed side by side. J. Fluid Mech. 246, 465–488.
Koch, D.L., Sangani, A.S., 1999. Particle pressure and marginal stability limits for a homogeneous monodisperse gas-fluidized bed: kinetic theory and numerical simulations. J. Fluid Mech. 400, 229–263.
Kumar, S., Hart, D.P., Brennen, C.E., 1990. Granular pressure measurements in fluidized beds. ASME Cavitation and Multiphase Flow Forum, June 1990, Toronto, Canada.
Lamb, H., 1945. Hydrodynamics, 6th ed. Cambridge Press, Cambridge, MA.
Liu, J.T.C., 1982. Note on a wave hierarchy interpretation of fluidized bed instabilities. Proc. Roy. Soc. London., A 380, 229–239.
Rahman, K., Campbell, C.S., 2001. Particle pressures generated around bubbles in gas-fluidized beds. J. Fluid Mech. (in press).
Richardson, J.F., Zaki, W.N., 1954. Sedimentation and fluidization: part I. Trans. Inst. Chem. Eng. 32, 35–53.
Rietema, K, 1991. The Dynamics of Fine Powders. Elsevier, London.
Sangani, A.S., Zhang, D.Z., Prosperetti, A., 1991. The added-mass, Basset, and viscous drag coefficient in nondilute bubbly mixtures undergoing small amplitude oscillatory motion. Phys. Fluids A. 3, 2955–2970.
Schügerl, K., Nerz, M., Fetting, F., 1961. Rheologische eigenshaften von gasdurchströmten Fliessbettsystemen. Chem. Eng. Sci. 15, 1–38.
Shook, C.A., Roco, M.C., 1991. Slurry Flow Principles and Practice. Butterworth-Heinemann, Boston, MA, p. 324.
Singh, P., Joseph, D.D., 1995. Dynamics of fluidized suspensions of spheres of finite-size, Int. J. Multiphase Flow 21, 1–26.
Thomas, D.G., 1965. Transport characteristic of suspension: viii, a note on the viscosity of Newtonian suspensions of uniform spherical particles. J. Colloid Int. Sci. 20, 267–277.
Wallis, G.B., 1969. One-dimensional Two-phase Flow. McGraw-Hill, New York, p. 408.
Yates, J.G., Cheesman, D.J., Sergeev, Y.A., 1994. Experimental observation of voidage distribution around bubbles in a fluidized bed. Chem. Eng. Sci. 49, 1885–1895.
Zenit, R., Hunt, M.L., Brennen, C.E., 1997. Collisional particle pressure measurements in solid-liquid flows. J. Fluid Mech. 353, 261–283.
Zhang, D.Z., Prosperetti, A., 1994. Averaged equations for inviscid disperse, two-phase flow. J. Fluid Mech. 267, 185–219.